Application of Mesh Modifications and Adjoint Error Estimates

S. Albensoeder

Abstract. Two methods for mesh modification are considered to improve hybrid meshes for CFD calculations. The first method is an adaptation with new sensors. The new sensors are based on an adjoint approach to calculate the sensitivity with respect to a goal function. Here the sensitivity of lift, drag and pitching moment was calculated with respect to the numerical dissipation terms. The second method is a local mesh modification of the unstructured part of the hybrid mesh based on an algebraic quality measure. For an a posteriori improvement the flow properties can be included to build a new anisotropic metric. Both new methods were applied to industrial relevant test cases.

1 Introduction

One problem of today computational fluid dynamics (CFD) is the discretization of the computational domain. Due to the limits of computational resources the discretization of the domain is not fine enough. Therefore the discretization can have a significant effect to the results.

A common approach to reduce this uncertainty is the adaptive refinement of the grid where errors occur. In the past several sensors (e.g. gradient based, reconstruction based) were developed to detect these underresolved regions. A sensor which computes the sensitivity of a discretization with respect to a specified goal function was introduced by [13]. The sensor was computed by solving an adjoint problem. One bottleneck of the method was that the final sensor was computed on the isotropic refined mesh instead of the original mesh. For complex configurations with a high number of grid points the demands to the computational resources are very high. In this investigation the sensors of [2] were used. This method computes the

S. Albensoeder

P3 Voith Aerospace GmbH, Flughafenallee 26, 28199 Bremen, Germany
e-mail: Stefan.Albensoeder@p3voith.com

sensitivity with respect to numerical dissipation terms. By this ansatz the error estimation can be done without any mesh refinement step.

Another approach is the improvement of a given mesh by local modifications. This improvement can be related to improve badly shaped elements and to orientate elements in the direction of the flow.

The uncertainty due to influences of the mesh generation drives the limitation that small influences can only be computed on the same or slightly modified mesh. One example is the deformation of the geometry due to aerodynamic loads. To reduce the uncertainty the whole mesh will be deformed to avoid a new meshing. Unfortunately this deformation can cause inverted elements which foreclose a new CFD computation. These cells have to be repaired which can also be done by the introduced local mesh modification.

In the next section the investigated methods are described. In section 3 the methods were applied to industrially relevant test cases. Finally a conclusion and an outlook are given.

2   Methods

For this study two different methods were used. The first approach solves an adjoint problem to get an error estimate of a functional. This error estimate is used as sensor for adaptation. The second method is based on the local modification of the unstructured part of the mesh to increase the quality of the mesh. All computations were performed with the TAU solver from the DLR (Deutsches Zentrum für Luft- und Raumfahrt).

2.1   Adjoint Error Estimation Method

The adjoint error estimation method uses a solution of an adjoint problem as sensor for an adaptation. The sensor is goal-oriented which means that for a specific goal function (e.g. C_L, C_D or C_{My}) the sensitivity on the error of this goal-function is locally computed. Based on this error estimate the mesh is refined to improve the results with respect to the specified goal function.

The original sensor of [13] is based on an estimate for the goal function I on a globally refined mesh

$$I_h\left(U_h^H\right) - I_h\left(U_h\right) \approx \left(\psi_h^H\right)^T R\left(U_h^H\right) \tag{1}$$

by the adjoint ψ times the residuum R of the flow U, where the subscript h means results on the isotropically refined mesh, the superscript H denotes an extrapolation from the coarse to the fine mesh. So on the right hand side of (1) the adjoint ψ is computed on the original mesh and extrapolated to the fine mesh. The flow quantity

U is extrapolated to the fine mesh. After that the residuum is calculated on the fine mesh from this extrapolated vector.

To avoid the extrapolotion and the calculation of the residuum on the fine mesh a new sensor was developed by [2]. The idea of [2] is to assume that the major part of the discretization error comes from the dissipation error. The error estimate is then given by

$$I(U_h) - I(U) \approx \psi^T \left(k^{(2)} \frac{\partial R}{\partial k^{(2)}} + k^{(4)} \frac{\partial R}{\partial k^{(4)}} \right). \tag{2}$$

The corrected value of the goal function is

$$I(U_h) \approx I(U) + \psi^T \left(k^{(2)} \frac{\partial R}{\partial k^{(2)}} + k^{(4)} \frac{\partial R}{\partial k^{(4)}} \right). \tag{3}$$

The related sensor for the adaptation is the absolute value of the local product

$$s_{i,j} = \left| \psi_{i,j}^T \left(k_{i,j}^{(2)} \frac{\partial R_{i,j}}{\partial k^{(2)}} + k_{i,j}^{(4)} \frac{\partial R_{i,j}}{\partial k^{(4)}} \right) \right|. \tag{4}$$

2.2   Mesh Manipulation

For optimizing a mesh, a quality measure for its elements has to be defined. Here the used quality measure based on the so-called *mean ratio*

$$q_i = \begin{cases} 4\sqrt{3} \cdot \dfrac{A_i}{\sum_{j=1}^{3} l_{ij}^2} & \text{for 2D meshes (triangles)} \\[4mm] 12 \cdot \mathrm{sign}\,(V_i) \cdot \dfrac{\sqrt[3]{(3V_i)^2}}{\sum_{j=1}^{6} l_{ij}^2} & \text{for 3D meshes (tetrahedron)} \end{cases}, \tag{5}$$

where A_i is the area, V_i the volume and l_{ij} the edge lengths of the element i (see figure 1a). Basically the measure is a ratio between the volume (3D) or area (2D) and the edge lengths.

For three-dimensional cases this quality measure was extended to pyramids by splitting the pyramid into four tetrahedra by introducing a mid point on the basis of the pyramid (see figure 1b).

The implementation of the mean measure allows to use local anisotropic metrics. The modified metric can be helpful if more information about the flow e. g. a preliminary solution is available. In this case the orientation of the elements to the local flow is considered. Due to this new metric the edge lengths, area and volume are measured in the space of the new metric $\mathcal{M}$. The size functions in the new metric are then given by
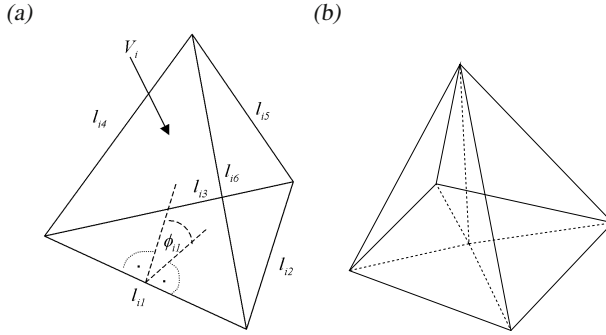
Fig. 1 *(a)* Nomenclature of variables on a tetrahedral element *i*. *(b)* Splitting of a pyramid into four tetrahedrons.

$$l_{ij}^{\mathscr{M}} = \sqrt{(\mathbf{x}_i - \mathbf{x}_j)^T \cdot \mathscr{M} \cdot (\mathbf{x}_i - \mathbf{x}_j)}, \tag{6}$$

$$A_i^{\mathscr{M}} = \sqrt{det(\mathscr{M})} \cdot A_i \quad \text{(for 2D meshes)}, \tag{7}$$

$$V_i^{\mathscr{M}} = \sqrt{det(\mathscr{M})} \cdot V_i \quad \text{(for 3D meshes)}. \tag{8}$$

For this study the metric was derived from the Hessian of the local Mach number Ma_{local}

$$\mathscr{H} = \frac{\partial}{\partial x_i \partial x_j} \text{Ma}_{local}. \tag{9}$$

To get a positive definite metric the Hessian was decomposed to its eigenvalues.

$$\mathscr{H} = \mathbf{R} \cdot \begin{pmatrix} \lambda_1 & 0 & 0 \\ 0 & \lambda_2 & 0 \\ 0 & 0 & \lambda_3 \end{pmatrix} \cdot \mathbf{R}^T. \tag{10}$$

The new local metric is then defined by the absolute values of the eigenvalues

$$\mathscr{M} = \mathbf{R} \cdot \begin{pmatrix} |\lambda_1| & 0 & 0 \\ 0 & |\lambda_2| & 0 \\ 0 & 0 & |\lambda_3| \end{pmatrix} \cdot \mathbf{R}^T \tag{11}$$

To improve the quality of a three-dimensional mesh, four different methods are implemented to modify the unstructured:

- edge swapping for up to 8 surrounding tetrahedrons [6, 10]
- face swapping [*face to edge swap* in 10]
- edge collapsing [9]
- combined smoothing [11, 1, 4] with an optimizer for not continuously differentiable goal functions [5, 6, 3]
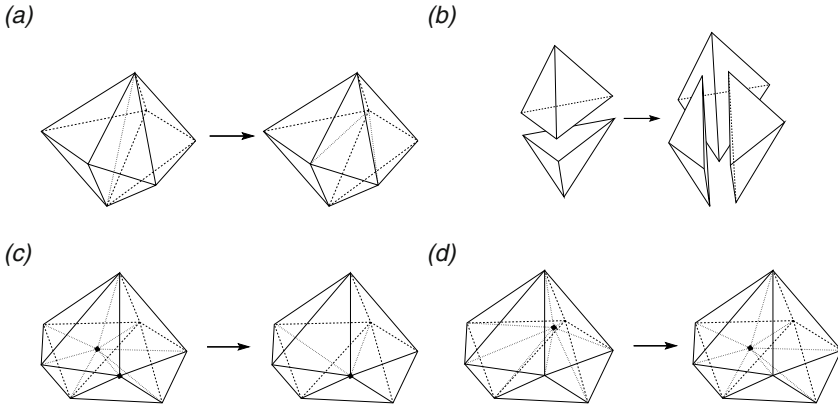
Fig. 2 Examples for *(a)* edge swapping, *(b)* face swapping, *(c)* edge collapsing and *(d)* combined smoothing

Each method modifies the mesh locally and acts on tetrahedrons. The combined smoothing and the edge collapsing were extended to allow modifications on points connected with pyramids. An example for each method is sketched in figure 2*(a)*–*(d)*. For two-dimensional grids only edge swapping and the movement of nodes are implemented.

For pointwise optimization due to movement of a node, a goal function has to be defined which combines the quality of surrounding elements S_i of a node i. Here the minimal quality

$$\bar{g}(S_i) = \min_{j \in S_i} q_j \qquad (12)$$

was used as goal function for the optimizer.

A modification of the grid is tried if the geometrical constraints allow a modification. Additionally the following demands have to be always fulfilled to accept a modification step:

- the minimal quality is larger than zero (to avoid inverted elements)
- the minimal quality is larger than the global minimal quality
- the goal function has to be improved (in the case of node movement)
- improve the mean quality (and therefore the global quality of the mesh)

3   Results

3.1   *Adaptation by an Adjoint Error Estimate*

The adjoint error estimate as sensor for adaptation is tested on two configurations. The first configuration is a clean wing/body configuration of the DLR-F6 geometry

[8, 12]. The second configuration is the high-lift wing/body configuration TC 217 with deployed flaps and slats. For both configurations the numerical results are compared to wind tunnel measurements.

3.1.1   DLR-F6

This test case was defined for the Third AIAA CFD Drag Prediction Workshop [see 12]. The flow parameters for the DLR-F6 wing/body configuration are $Ma \approx 0.75$, $Re \approx 5 \cdot 10^6$ and $T_{ref} = 322.22$. The meshes were taken from the workshop[1].

The first test on this configuration is a comparison of a mesh refinement study and an adaptation series with the new sensors. For the refinement study a computation on a coarse ($N_P = 2464385$), a medium ($N_P = 5102446$) and a fine ($N_P = 8535263$) mesh was performed. For all computations the lift is targeted to $C_L = 0.5$ and the Spalart–Allmaras turbulence model was used. Outgoing from the coarse mesh the adaptation was repeated five times with the new sensor given in equation (4). The number of points increases within each adaptation step by 30%. Additional to the flow computation in each adaptation step the adjoint error estimation was computed.

The values of the angle of attack α, the drag C_D and the pitching moment C_{My} of the refinement study are plotted in figure 3(a)–(c) as function of $N_P^{-2/3}$. The crosses show the results of the coarse, medium and fine mesh. The circles and squares connected by solid lines are showing the results of the adaptation with the new sensors for lift and drag, respectively. Signs connected by dotted lines denote values which are corrected by the adjoint error estimate (3). The results from the refined meshes show an ambiguous behaviour regarding the convergence for all plotted coefficients. In contrast the results from the adaptation series converge approximately to distinct values. The corrections by the adjoint error estimate decrease continuously so that finally the corrected values converge to the uncorrected values. The values of the finest meshes of the adaptation series are higher than the values from the finest mesh, e. g. $\Delta C_D \approx 10DC$.

A comparison with the results given in [12] shows that the results of the refined and of the adapted meshes are lying in the range of other codes. Additionally [12] make a statistical analysis of the values for drag. Their estimate for the mean of the drag is $C_D = 0.0269$, the standard deviation is $\sigma = 0.0006$. Here the values of the adaptation are significantly out of this range.

The experimental results are taken from [7]. The measured values are shown in figure 3(a)–(c) by a dashed line. For the angle of attack and the pitching moment the adapted grids are lying closer to these experimental results than the results of the refined meshes. For the drag the values on the refined meshes are closer to the experiment.

In the second test a polar is computed. Again the flow conditions are $Ma \approx 0.75$, $Re \approx 5 \cdot 10^6$ and $T_{ref} = 322.22°K$. Instead of a fixed target lift coefficient here the angle of attack was varied in the range of $\alpha = [-5°, 2°]$. The polar is computed on

---

[1] See http://aaac.larc.nasa.gov/tsab/cfdlarc/aiaa-dpw
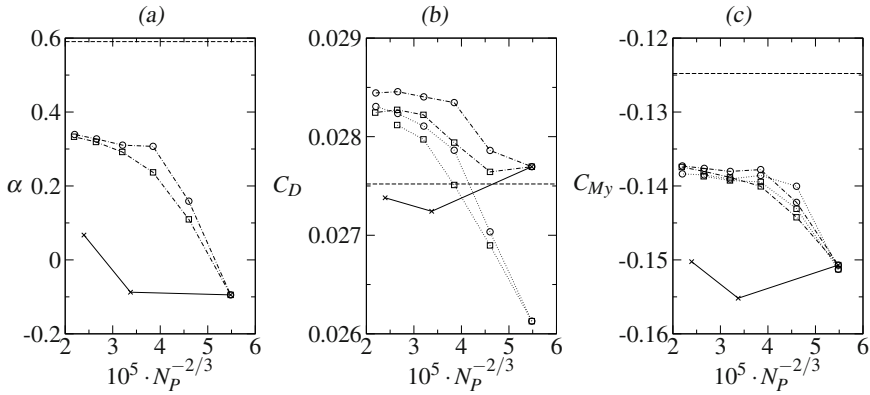
Fig. 3 Angle of attack α (a), drag C_D (b) and the pitching moment C_{My} (c) as function of the grid points N_P for the DLR-F6 model. The lift is kept constant to $C_L = 0.5$. $\times$ denotes the result on the base meshes. $\circ$ and $\square$ connected by a dash-dotted line marks the results of the adaptation with an adjoint sensor with a sensitivity to lift and drag, respectively. The results connected with the dotted lines are corrected by the adjoint error estimate. The dashed line denotes the experimental results taken from [7].

the coarse, medium and fine mesh. To avoid the computation of an adjoint solution for each angle of attack, four adapted meshes from the previous adaptation series for lift and drag are used. Here the mesh from the first (*ad1*) and the third adaptation (*ad3*) step with $N_P \approx 3.2 \cdot 10^6$ and $N_P \approx 5.5 \cdot 10^6$ are chosen, respectively.

In figure 4(a) the lift is plotted as function of the angle of attack α. The results on the coarse, medium and fine mesh are denoted by $\circ$, $+$ and $\ast$. On the coarse and medium mesh the results are similar. On the fine mesh the slope is lower than on the coarser meshes. The computed lift on the adapted meshes *ad1* for lift and drag are nearly identical within the line thickness. In comparison to the fine mesh the lift is shifted by $\delta C_L \approx 1LC$. The computed lift on the meshes *ad3* show the same behaviour. Only the shift to the fine mesh is $\delta C_L \approx 2LC$.
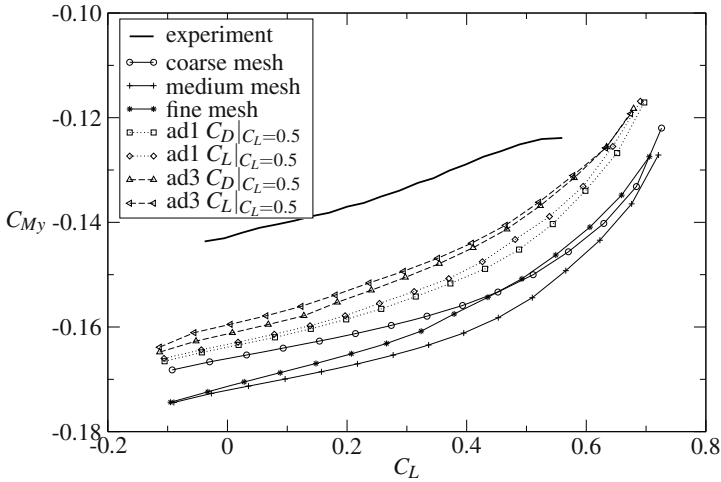
The lift as function of the drag is plotted in figure 4(b). On the refined mesh series the drag reduces by the mesh refinement. The strongest variation of the lift as function of the drag is observable in the region of minimal drag where the curve of the fine mesh is shifted to the left by $\delta C_D \approx 10DC$ in comparison to the drag computed on the coarse mesh. For large angles of attack the reduced drag is nearly completely compensated by the reduced values of the lift so that the curves of the refinement series are close together. For the adapted meshes the shift at the minimal drag is only $\delta C_D \approx 3 - 5DC$ with respect to the results on the coarse mesh. In contrast to the refined meshes the deviation for large angles of attack are getting higher by the number of points.

In figure 5 the pitching moment is plotted as function of the lift. The results for the refined mesh series are ambiguous and no trend is observable. The pitching moment on the adapted meshes *ad1* and *ad3* increases by each refinement.

(a)

(b)
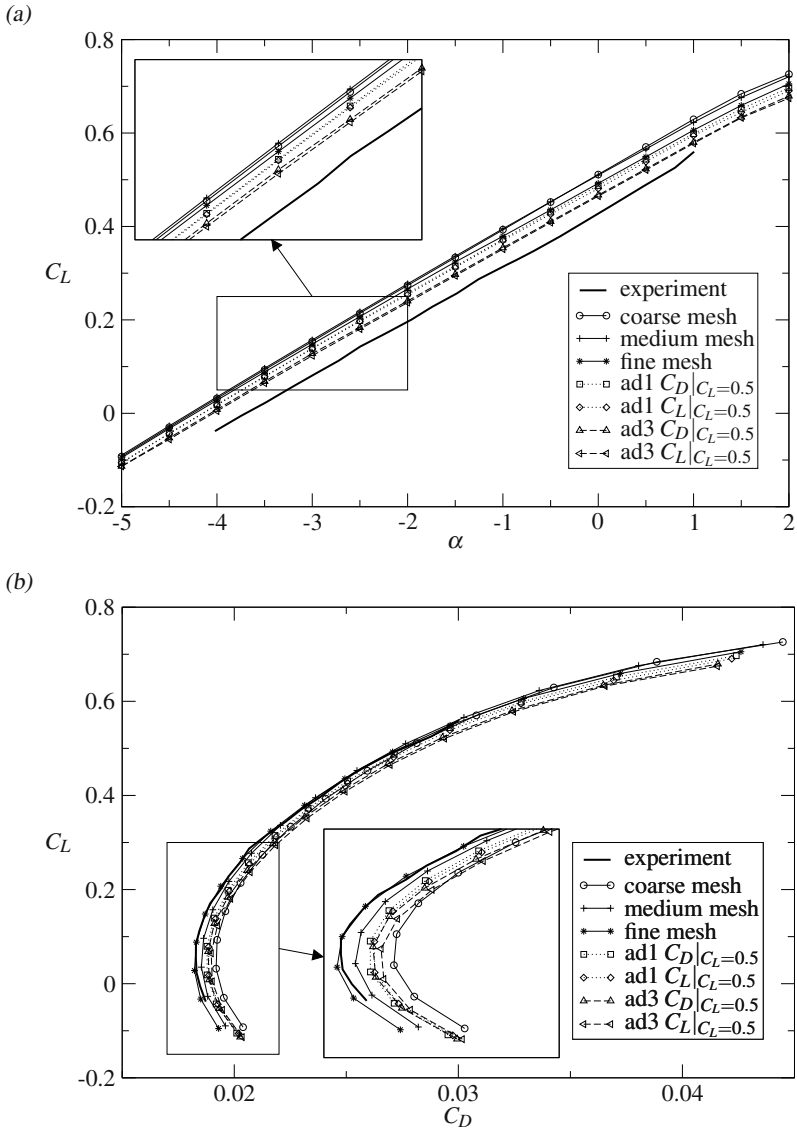
Fig. 4 *(a)* Lift C_L as function of the angle of attack α and *(b)* polar of C_L as function of C_D for the DLR-F6 model. $\circ$, $+$ and $*$ denotes the results on the coarse, medium and fine mesh. $\square$ and $\diamond$ marks the results on the first adapted mesh at $C_L = 0.5$ with respect to the lift and drag, respectively. $\triangle$ and $\triangleleft$ denotes the results computed on the meshes of the third adaptation step of figure 3. The solid line denotes the experimental results taken from [7].

Fig. 5 Pitching moment C_{My} as function of the lift C_L for the DLR-F6 model. The labels are identical to the labels of figure 4.

The measurements of [7] are plotted in the figures 4 and 5 as a solid line. Like in the convergence study by trend the lift (angle of attack) and pitching moment of the adapted meshes fits more to the experimental results than the coefficients computed on the refined meshes. The measured lift as function of the drag fits more to the refined meshes.

3.1.2 TC 217

The adaptation sensor based on an adjoint error estimate is also applied to the second test case of the TC 217 high-lift configuration. The model was a wing/body configuration with deployed slat and flaps. The geometry was previously used in the EURO-LIFT project. The flow parameters are $Ma \approx 0.18$, $Re \approx 1.5 \cdot 10^7$ and $T_{ref} \approx 114°K$. All computations are performed with the Spalart–Allmaras turbulence model.

For this configuration the polar was computed on a mesh with $N_P = 10733766$ grid points. Outgoing from this mesh for several angles of attack an adaptation with the new sensor (4) was performed. Like for the DLR-F6 model the adaptation was repeated several times. The number of points increases within each adaptation step by 30%. In contrast to the DLR-F6 test case convergence problems occur on this configuration, e.g. the convergence was too slow and the computational effort too high or the adjoint computation diverges. However, for most of the angles of attack one adaptation iteration was successfully performed. In figure 6 the results of this first test were plotted. The + shows the result of the computation on the base mesh. The corresponding experimental values were plotted as solid line. The major differences are observable in the linear region and near the maximal value of lift $C_{L,max}$.

(a)
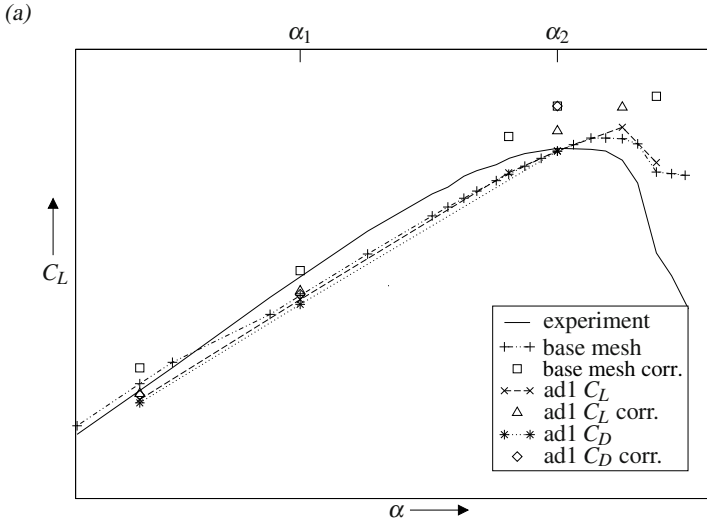
Fig. 6 Lift C_L as function of the angle of attack α for the TC-217 model. $+$ and $\circ$ denote the results on the base mesh and the corrected values by the adjoint error estimation, respectively. $\times$ and $*$ mark the results of the first adaptation step with a sensor based on lift and drag, respectively. The $\triangle$ and $\diamond$ are the corrected values. The solid line denotes the experimental results.

For lower angles of attack the computational results have a step-like shape. On the other side of the curve the angle of attack and the corresponding lift is too high. The values of the lift corrected by the adjoint error estimate ($\square$ in figure 6) are higher then the original ones.

Outgoing from these results the mesh was adapted for several angles of attack α with the adjoint error estimate for lift ($\times$ in figure 6) and drag ($*$ in figure 6), respectively. For both sensors an improvement of the linear region is observable. The step like behaviour vanishes. In the nonlinear region the results (if they are available) are similar to the results on the base mesh. The corrected values for the adapted grids are higher than the original values. Unfortunately most of the adjoint computations fail. Due to this experiment and the high computational effort four adapted meshes are selected from the linear and the nonlinear region. The four selected meshes are the meshes adapted by the lift or drag sensor for $\alpha = \alpha_1$ and $\alpha = \alpha_2$ (see figure 6), respectively. The results are plotted in figure 7. The results on the base mesh are marked by $+$. The results of the lift adapted mesh at α_1 and α_2 are denoted by $\circ$ and $\square$, respectively. The results of the drag adapted meshes are denoted by $\triangle$ and $\times$.

In figure 7(a) the lift is plotted as function of the angle of attack. In the linear region the values on the adapted meshes are close together. The deviation between the meshes *ad1* C_{L,α_1} and *ad1* C_{D,α_1} is $\delta C_L \approx 1LC$. The offset between the meshes *ad1* C_{L,α_2} and *ad1* C_{D,α_2} is of the same order. The offset between the adapted meshes and the base mesh is about $\delta C_L \approx 10LC$ for $\alpha \lesssim \alpha_1$. The step like behaviour in the lift curve at $\alpha \approx \alpha_1$ vanishes due to the adaptation. In the nonlinear region

close to maximal lift the results of the adapted meshes diverge from each other. The results on the meshes which are adapted at α_2 show a higher maximal lift coefficient ($\delta C_L \approx 3LC$ with respect to the base mesh) and also the angle of attack of maximal lift is shifted by $\delta\alpha \approx 1°$ relative to the results on the base mesh. The maximal lift value on the meshes adapted in the linear region at α_1 have a lower value than the lift on the base mesh. The offset in the position of the maximal lift is $\delta\alpha \approx 0.5°$.

In figure 7(b) the lift is plotted as function of the drag. Again the results on the adapted meshes are close together in the linear region. At maximum lift the results on the meshes adapted at α_1 diverge from the values of the meshes adapted at α_2.

All computations differ from the experimental results. The slope of $C_L(\alpha)$ is lower for the computational results than in the experiment. The values of maximal lift are higher than in the experiment. The same holds for $C_L(C_D)$ in figure 7(b). However, in the linear range an improvement by the new method is observable due to the vanishing of the step like behaviour in the linear region. The improvements for the maximal lift are ambiguous.

3.2   Mesh Manipulation

3.2.1   Repairing of Meshes

Negative elements occur many times by applying a deformation on the mesh, e. g. for CFD/CSM coupling. The appearance of negative cells permits a CFD computation on those grids. To avoid a new meshing of the deformed geometry and to measure effects below the uncertainties of mesh effects the negative cells have to be repaired. Here the repairing of negative elements was successfully demonstrated on two configurations. An isotropic metric was chosen to calculate the quality measure.

The first test case was a clean wing/body configuration with horizontal tail planes. To trim the configuration the horizontal tail plane was deformed. Due to deformation of the tail plane 83 elements with a negative volume occur (figure 8). These inverted elements are tetrahedrons and pyramids. By applying the mesh modification all negative elements vanish.

The second test case was a commercial aircraft including wing, body, nacelle, pylon, vertical tail plane and flap track fairings in a high-lift configuration (figure 9a). Due to the applied deformation, 26 tetrahedrons have a negative volume. These elements are located in the slot between the flap inboards and the wing (figure 9b). Again, by applying the implemented mesh modification all negative tetrahedrons are inverted to valid elements with a positive volume.

In many cases the generation of negative elements can also be prevented by applying the mesh modification on elements with a low quality before the mesh is deformed. For example in the previous case of trimming the horizontal tail plane, negative elements were prevented if the mesh was improved before the deformation step is performed.

(a)

(b)
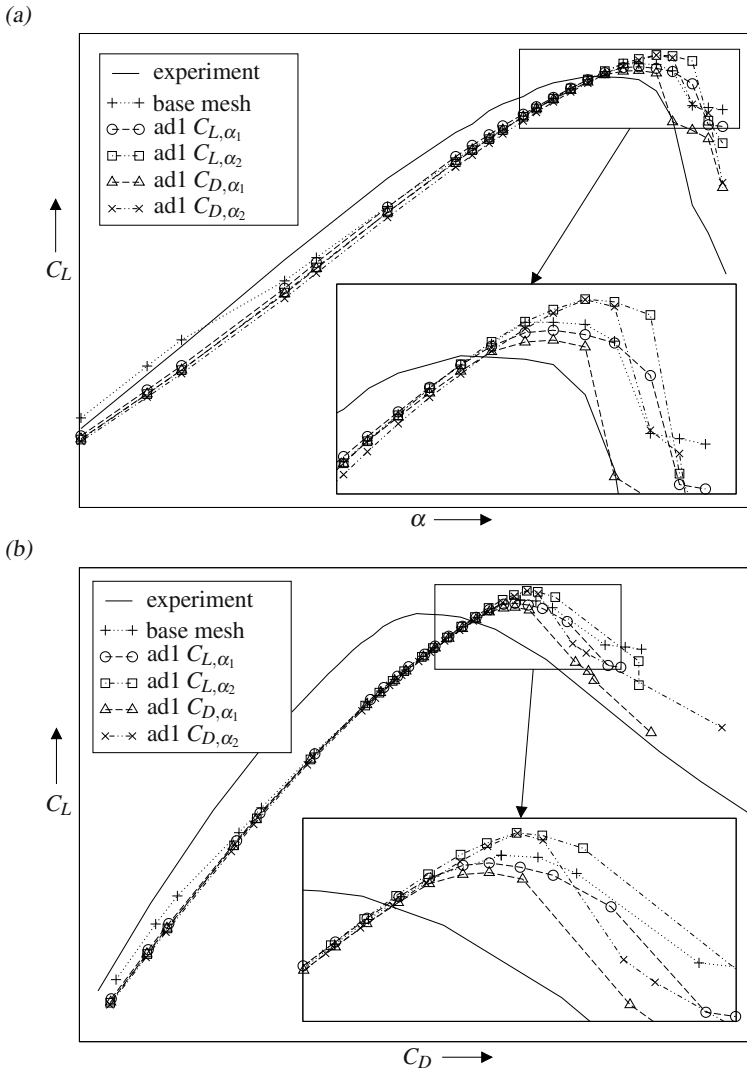
Fig. 7 *(a)* Lift C_L as function of the angle of attack α for the TC-217 model. *(b)* Polar for C_L and C_D of the TC-217 model. $+$ marks the results computed on the base mesh. $\circ$ and $\square$ denote the results of the meshes adapted with the adjoint lift sensor for α_1 and α_2. $\triangle$ and $\times$ show the results for the adapted grids with respect to the drag. The solid line shows the experimental results.

(a) *(b)*
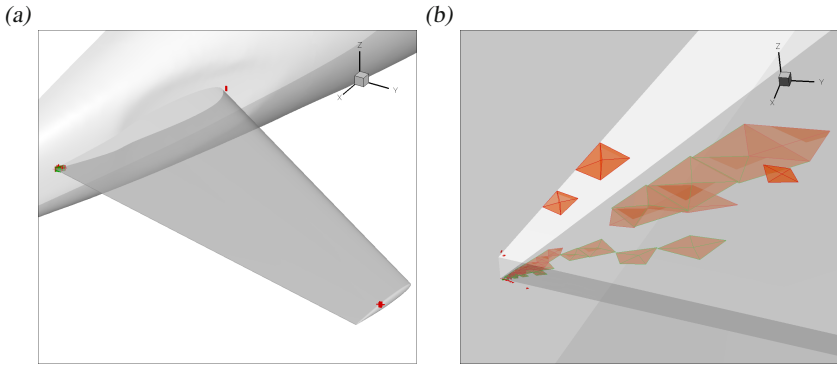
Fig. 8 *(a)* Negative pyramids and tetrahedrons near by a deformed tail plane. *(b)* Detail of *(a)*.

(a) *(b)*
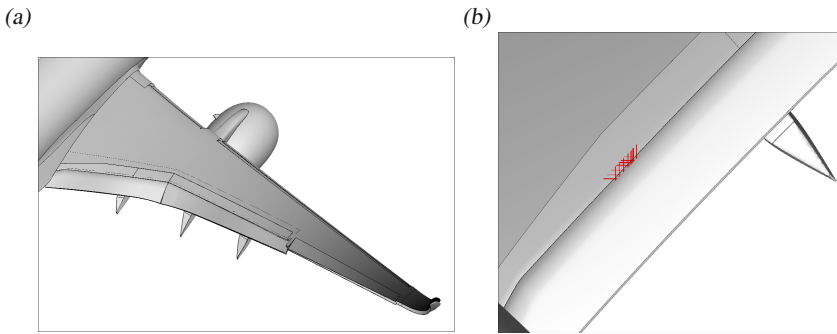
Fig. 9 *(a)* Deformed wing in a high-lift configuration. Shown is the original wing and the deformed wing. Darker regions have a higher deformation. *(b)* Detail of *(a)* with shown negative elements marked by crosses.

Another application of the mesh modification is the improvement of the quality of the unstructured part of the mesh when the computation on the mesh diverges. In figure 10*(a)* an example is shown where many tetrahedrons have a bad shape. By applying the mesh modifications the number of badly shaped elements decreases significantly (figure 10*b*). The number of tetraherons with a dihedral angle less than one degree decreases from $N_{\xi<1^\circ} = 6840$ to $N_{\xi<1^\circ} = 29$. The number of tetraherons with a dihedral angle less than five degree decreases from $N_{\xi<1^\circ} = 34598$ to $N_{\xi<1^\circ} = 252$. Note that after the improvement of the mesh a converged CFD solution could be achieved.

*(a)*   *(b)*
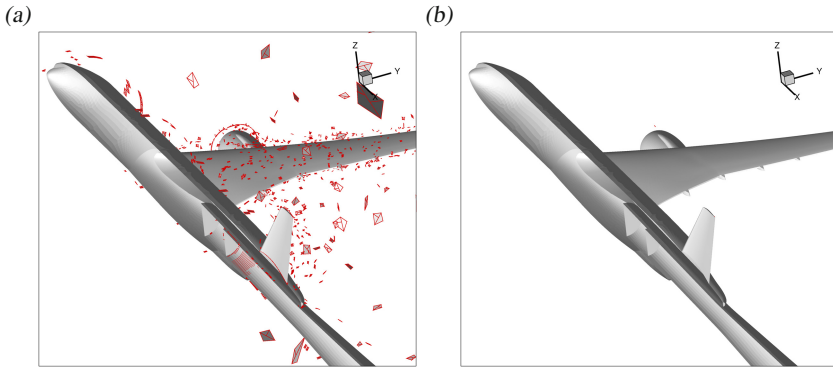
Fig. 10 Mesh with many badly shaped tetrahedral elements before *(a)* and after *(b)* the mesh modification. In both figures elements with a dihedral angle less than one degree are shown.

3.2.2   Mesh Modification with Anisotropic Quality Measures

The mesh modification was applied to the DLR-F6 test case described in section 3.1.1 to see the influences on the aerodynamic coefficients. Again a target lift computation for $C_L = 0.5$ was performed. After the flow computation the coarse, medium and fine mesh was modified by using a quality measure which uses an anisotropic metric. The metric was derived from the Hessian of the local Mach number. The flow was recomputed on the anisotropic mesh. This procedure was performed twice.

In figures 11*(a)*–*(c)* the angle of attack, the drag and the pitching moment are plotted as function of the grid points N_P. The results computed on the base meshes are denoted by ×. The results of the first and second mesh modification step is marked by ∘ and □. The major improvements are observable for the drag on the coarse mesh, but the differences to the original mesh are relatively small in comparison to the changes caused by an adaptation with the new sensors. The major changes are observable in the resolution of the wake. In figure 12 the eddy viscosity is shown on four different meshes. The eddy viscosity on the coarse and fine base meshes (figure 12*a,c*) dissipates in the unstructured part very quickly, where on the anisotropically modified meshes (figure 12*b,d*) the wake is more resolved behind the wing, even on the coarse mesh. The improved wake resolution is observerable on the whole configuration.

In a second test the mesh modification with an anisotropic quality measure was applied to the TC-217 configuration (see section 3.1.2). For the test the mesh modification with the anisotropic quality measure was applied twice to the base mesh for $\alpha = \alpha_1$. Again the metric was derived from the Hessian of the local Mach number. The results are presented in figure 13. The + and □ denote the results on the original and the modified mesh, respectively. Due to the mesh modification the lift decreases
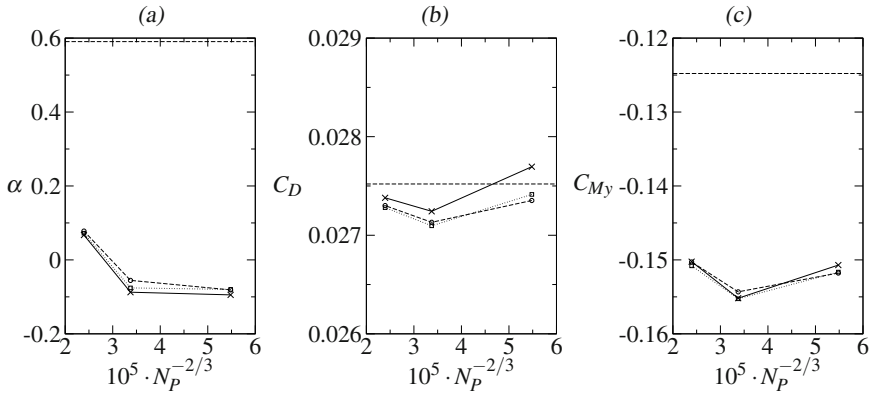
Fig. 11 Angle of attack α (a), drag C_D (b) and pitching moment C_{My} (c) as function of the grid points N_P for the DLR-F6 model. The lift is kept constant to $C_L = 0.5$. $\times$ denotes the result on the base meshes. $\circ$ and $\square$ mark the results on the meshes modified once and twice by the modification with an anisotropic quality measure, respectively. The dashed line denotes the experimental results taken from [7].

by $\delta C_L \approx 8LC$. The drag increases by $\delta C_D \approx 100DC$. The result on the modified mesh increases the differences to the experimental results.

4 Conclusion

The methods of adjoint error estimates and local mesh modification are applied to several test cases. The main focus was set on the global aerodynamic coefficients. Only for the mesh repairing the focus was set on the validity and the computablility of meshes.

For the adaptation series of the DLR-F6 with the adjoint error estimates no final conclusion can be given. The numerical values given by [12] are widely spread. The corresponding experimental data show for some coefficients improvements and for some not. At least one should note that a comparison of the experimental results for $Re = 3 \cdot 10^6$ measured in the NASA NTF and in the ONERA S2MA facility shows as well differences especially in the drag [7]. If one projected these differences to the measurements at $Re = 5 \cdot 10^6$ the adapted meshes would show an improvement for all coefficients.

However, the results of the adaptation series converge for both used sensors to similar values which are different from the values of the finest mesh. The results on the meshes which are locally modified to satisfy a quality measure based on an anisotropic metric are close to the results computed on the original meshes.

For the high-lift configuration the adjoint approach improves the results in the linear region of the polar. The values of maximal lift are ambiguous and depend on the used meshes. The deviations of the results on the meshes which are optimized to

(a)

(b)

(c)

(d)
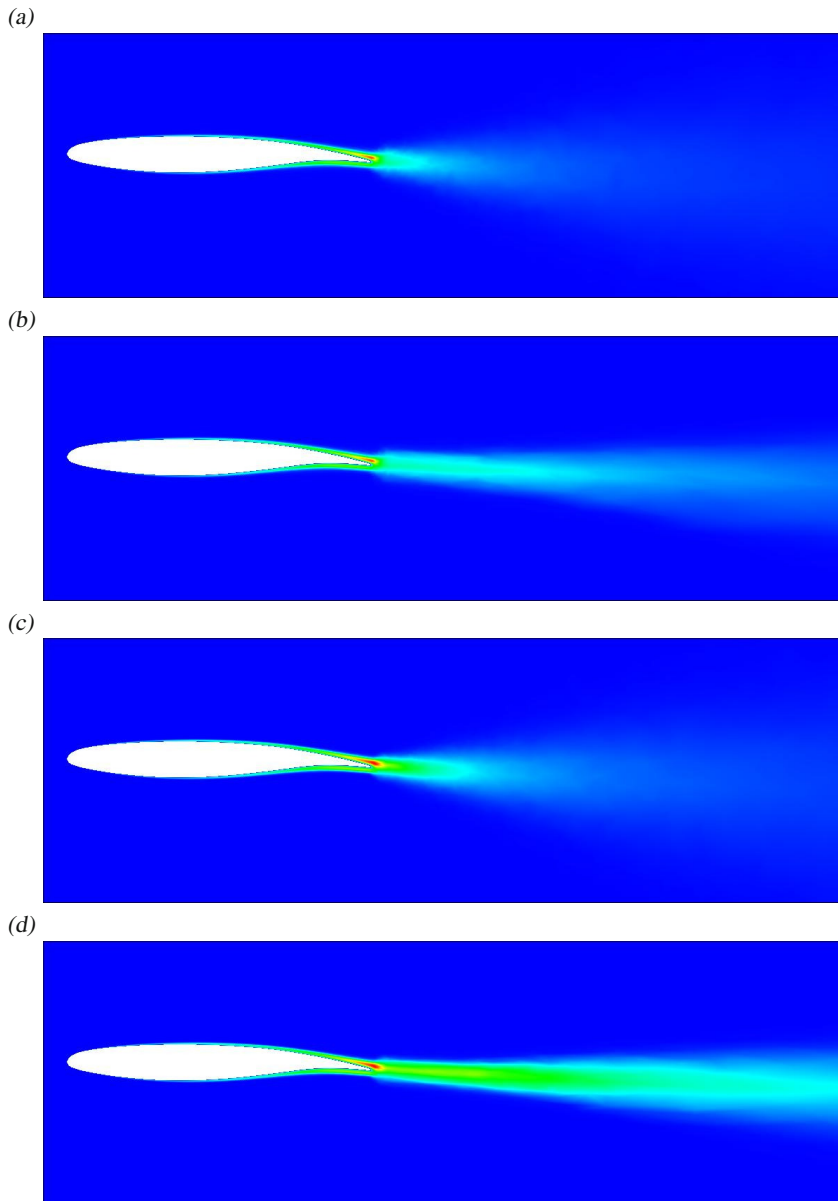
Fig. 12 Eddy viscosity of the wake at $\eta = 0.514$ for *(a)* the base coarse mesh, *(b)* the aniso-tropic coarse mesh, *(c)* the base fine mesh and *(d)* the anisotropic fine mesh of the DLR-F6 configuration

(a)

(b)
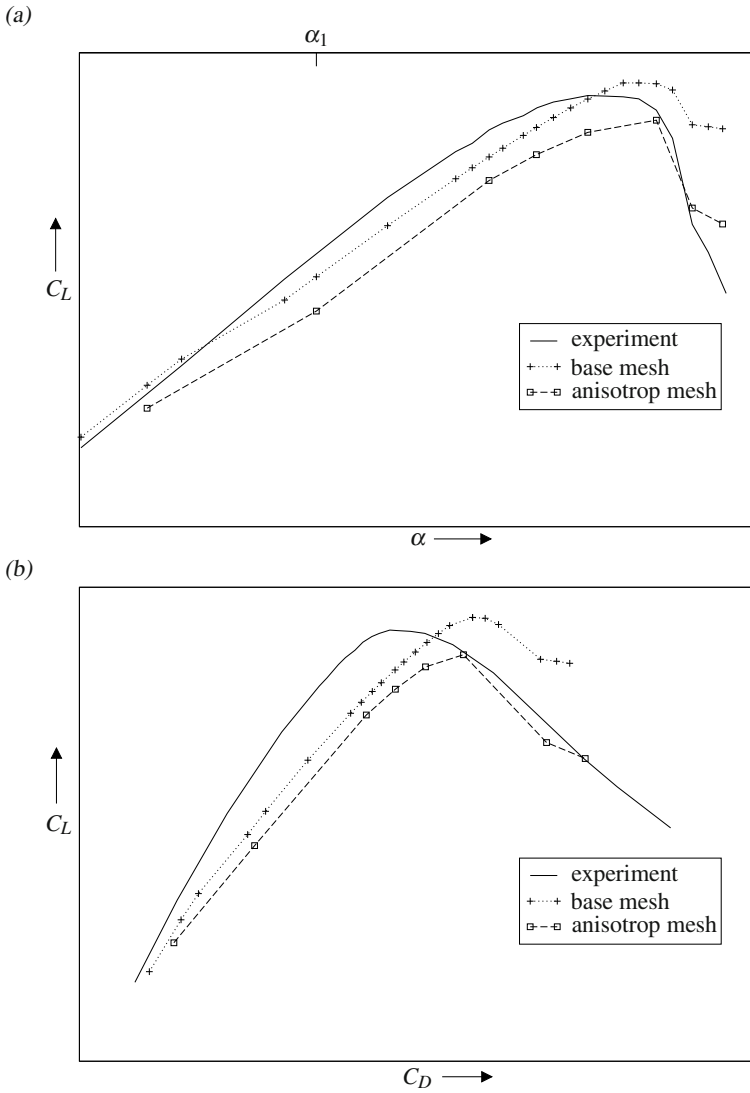
Fig. 13 *(a)* Lift C_L as function of the angle of attack α for the TC-217 model. *(b)* Polar for C_L and C_D of the TC-217 model. $+$ marks the results computed on the base mesh. $\square$ denotes the results on the modified meshes. The solid line shows the experimental results.

an anisotropic quality measure increase. The reason for the strong deviations have to be analyzed.

The results for the adjoint approach show additionally that the strategy to use one grid for the whole polar works even if the adaptation was performed only for a specific angle of attack. This strategy reduces significantly the computational effort and makes the adjoint approach applicable.

The repairing of meshes was successfully demonstrated for several meshes. This method is useful if a computation on a mesh due to numerical errors or negative elements fails and a new mesh generation is not desirable.

5   Outlook

[13] couples the adjoint adaptation with the feature of anisotropy. He demonstrated that with this mixed approach the convergence of the coefficients is much faster than with an isotropic mesh adaptation. [13] states that the adjoint approach balances the inaccuracies which can occur by the anisotropic meshes and uses the positive effects of anisotropic meshes. This has to be tested with the present methods.

Additionally the introduced error estimation approach of [2] tries to reduce the error with respect to numerical dissipation terms. The original work of [13] tries to reduce the error with respect to the discretization itself. A comparison of both approaches would also be interesting.

References

[1] Canann, S.A., Tristano, J.R., Staten, M.L.: An approach to combined Laplacian and optimization-based smoothing for triangular, quadrilateral, and quad-dominant meshes. In: 7th International Meshing Roundtable, Dearborn, Michigan, pp. 479–494. Sandia National Labs (1998)

[2] Dwight, R.: Heuristic a posteriori estimation of error due to dissipation in finite volume schemes and application to mesh adaptation. J. Comp. Phys. 227, 2845–2863 (2008)

[3] Freitag, L., Jones, M., Plassmann, P.: A parallel algorithm for mesh smoothing. SIAM J. Sci. Comput. 20, 2023–2040 (1999)

[4] Freitag, L.A.: On combinig Laplacian and optimization-based mesh smoothing techniques. ASME 220, 37–43 (1997)

[5] Freitag, L.A., Ollivier-Gooch, C.: A comparison of tetrahedral mesh improvement techniques. In: Proceedings of the Fifth International Meshing Roundtable, pp. 87–100. Sandia National Laboratories, Albuquerque (1996)

[6] Freitag, L.A., Ollivier-Gooch, C.: Tetrahedral mesh improvement using swapping and smoothing. Int. J. Numer. Meth. Engrg. 40, 3979–4002 (1997)

[7] Gatlin, G.M., Rivers, M.B., Goodliff, S.L., Rudnik, R., Sitzmann, M.: Experimental investigation of the DLR-F6 transport configuration in the National Transonic Facility. In: 26th AIAA Applied Aerodynamics Conference, Honolulu. American Institute of Aeronautics and Astronautics, Hawaii, AIAA 2008-6917 (2008)

[8] Laflin, K.R., Klausmeyer, S.M., Zickuhr, T., Vassberg, J.C., Wahls, R.A., Morrison, J.H., Brodersen, O.P., Rakowitz, M.E., Tinoco, E.N., Godard, J.L.: Data summary from Second AIAA Computational Fluid Dynamics Drag Prediction Workshop. J. Aircraft 42, 1165–1178 (2005)

[9] Li, X., Shephard, M.S., Beall, M.W.: 3D anisotropic mesh adaptation by mesh modification. Comput. Methods in Appl. Mech. Engrg. 194, 4915–4950 (2005)

[10] Pain, C.C., Umpleby, A.P., de Oliveira, C.R.E., Goddard, A.J.H.: Tetraherdral mesh optimization and adaptivity for steady-state and transient finite element calculations. Comput. Methods in Appl. Mech. Engrg. 190, 3771–3796 (2001)

[11] Shephard, M.S., Georges, M.K.: Automatic three-dimensional mesh generation by the finite octree technique. Int. J. Numer. Meth. Engrg. 32, 709–749 (1991)

[12] Vassberg, J.C., Tinoco, E.T., Mani, M., Brodersen, O.P., Eisfeld, B., Wahls, R.A., Morrison, J.H., Zickuhr, T., Laflin, R., Mavriplis, D.J.: Summary of the third AIAA CFD Drag Prediction Workshop. In: 45th AIAA Aerospace Sciences Meeting and Exhibit, Reno, Nevada. American Institute of Aeronautics and Astronautics, AIAA 2007-260 (2007)

[13] Venditti, D.A.: Grid adaptation for functional outputs of compressible flow simulations. PhD thesis, Massachusetts Institute of Technology, Boston, USA (2002)